

Tunable Circular Dichroism by Photoluminescent Moiré Gratings

Olha Aftenieva, Max Schnepf, Börge Mehlhorn, and Tobias A. F. König*

In nanophotonics, there is a current demand for ultrathin, flexible nanostructures that are simultaneously easily tunable, demonstrate a high contrast, and have a strong response in photoluminescent polarization. In this work, the template-assisted self-assembly of water-dispersed colloidal core-shell quantum dots into 1D light-emitting sub-micrometer gratings on a flexible substrate is demonstrated. Combining such structures with a light-absorbing metallic counterpart by simple stacking at various angles results in a tunable Moiré pattern with strong lateral contrast. Furthermore, a combination with an identical emitter-based grating leads to a chiroptical effect with a remarkably high degree of polarization of 0.72. Such a structure demonstrates direct circular polarized photoluminescence, for the first time, without a need for an additional chiral template as an intermediary. The suggested approach allows for reproducible, large-area manufacturing at reasonable costs and is of potential use for chiroptical sensors, photonic circuit applications, or preventing counterfeit.

nanosphere,^[8] or imprinting lithography.^[9] These approaches result in large-area quasicrystal patterns, being, however, permanently inscribed in the medium and, thus, hindering the tunability of optical properties. An alternative strategy implies separate manufacturing of periodic structural components and generating a Moiré interference by bringing them into close contact. The simplest periodic structures to consider are 1D gratings that, when stacked at various angles, result in two-and-a-half-dimensional chiral metasurface. Such structures demonstrate strong circular dichroism (CD). With crossed gold gratings, one could achieve CD, characterized through the degree of polarization, of 0.3.^[10] When using aluminum helically stacked lattices, the abovementioned effect was 2.5 times stronger and observed over the entire visible and near-infrared wave-

lengths range.^[11] By taking advantage of the surface lattice resonance from the metal nanoparticle arrangements, one can reach comparable effect strength.^[12] Such metal-based chiral structures, however, suffer from the non-radiative ohmic losses that limits their usage to the absorption-based applications.

To exploit the chiroptical effect for the light generation, one has to introduce a light-emitting component. Colloidal quantum dots (QDs) appear to be the optimal candidates, featuring broadband absorption, size- and material-controllable emission wavelength, high quantum yields, and photostability.^[13,14] To directly induce the circularly polarized photoluminescence, two principal strategies have been suggested: through connecting chiral ligands to the QDs surface^[15] or by combining achiral QDs with chiral plasmonic metasurfaces. The first approach resulted in relatively weak induced chirality and required elaborate surface modifications. On the contrary, combination with chiral metal nanostructures enabled strong circularly polarized emission. For this, the CD response of the template should match either absorption^[16] or emission bands of the QDs.^[17]

The necessity to have a chiral plasmonic template with inherent energy losses and quenching effects hinders such light-emitting metasurfaces from practical applications. On the contrary, assembling emitters into chiral structures directly enables loss-free polarized photoluminescence. On this notion, special care must be taken about the optical performance. To avoid significant quenching of the photoluminescence for closely packed QDs,^[18] one can utilize the core-shell QDs, where the distance between the emitting centers is defined by the shell thickness.^[19] Moreover, to match multiple virtual hybridization


1. Introduction

A Moiré effect occurs when repetitive structures such as gratings are superimposed against each other with a relative difference in lattice constant or in-plane rotation angle.^[1] By tuning these parameters, Moiré pattern can be accurately controlled and applied for measuring strain deformation,^[2] precise alignment in optical security labels,^[3] and biosensors.^[4] In addition, configurations with the Moiré effect show more optical features than their primary components.^[5] Formation of Moiré pattern can be realized through interference,^[5,6] block copolymer,^[7]

O. Aftenieva, Dr. M. Schnepf, B. Mehlhorn, Dr. T. A. F. König
Leibniz Institute for Polymer Research Dresden e.V.
Hohe Straße 6, 01069 Dresden, Germany

B. Mehlhorn
Leibniz Institute for Solid State and Materials Research Dresden e.V.
Helmholtzstraße 20, 01069 Dresden, Germany

Dr. T. A. F. König
Center for Advancing Electronics Dresden (cfaed)
Technische Universität Dresden
01062 Dresden, Germany
E-mail: koenig@ipfdd.de

 The ORCID identification number(s) for the author(s) of this article can be found under <https://doi.org/10.1002/adom.202001280>.

© 2020 The Authors. Advanced Optical Materials published by Wiley-VCH GmbH. This is an open access article under the terms of the Creative Commons Attribution License, which permits use, distribution and reproduction in any medium, provided the original work is properly cited.

DOI: 10.1002/adom.202001280

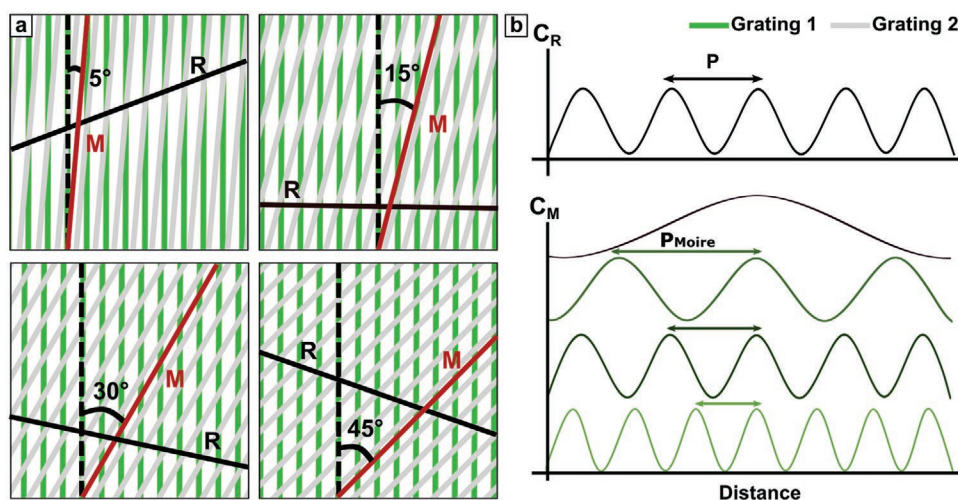


Figure 1. Exemplary interference patterns and their characterization. a) Moiré patterns generated by two superimposed gratings (as shown with green and gray lines) with equal periodicities at various orientation angles. b) Contrast profile plots along principal directions (*M*: crossing the Moiré interference lines; *R*: parallel to them).

states created by the Moiré pattern and observe a chiral response over a large wavelength span, it might be beneficial to employ emitters with broadband absorption, as well as emission, spectra.^[16,20]

Until now, production of periodic light-emitting structures with the features on the scale of the emitter wavelength remained to be challenging, and the direct arrangement of emitters into chiral structures providing a pure circular-polarized light-emitting device has not been demonstrated. Template stripping^[20,21] and electron beam lithography^[22] techniques potentially allow for high-resolution patterning, being, however, cost-inefficient and not applicable for large-area manufacturing. To produce patterned emitter-based structures on a centimeter-scale area, simple casting, Langmuir–Blodgett deposition, dip coating, inkjet printing, or photopatterning could be applied. However, these methods mostly result in films without sufficient uniformity and control over the film thickness.^[23–25] As an alternative, one can employ contact printing techniques^[26–29] to create periodic micrometer-sized structures on a centimeter scale through the confinement self-assembly of nanocrystals just by using a structured stamp. However, due to the generally poor cohesion of quantum emitters and the strong influence of artifacts on the wetting behavior, it remains a difficult task to assemble quantum emitters into a sub-micrometer grating.

To overcome this challenge, one has to adjust the surface properties of the stamping template, and utilize particles with a size much smaller than the gap. The latter is easily fulfilled for the QDs that are few nanometers in diameter. To allow the water-based colloidal solution to fill the gaps in the structured template, the contact angle must be sufficiently decreased through the surface activation. The stability of colloidal QDs in an aqueous solution is ensured, in this case, by thioglycolic acid (TGA) through the electrostatic repulsion of carboxylic groups,^[30] that additionally promote stronger adhesion of QDs to the substrate than to the stamping template. Then, during drying, van der Waals forces cause a strong cohesion between the particles. Overall, the abovementioned printing technique creates emitter-based sub-micrometer metasurfaces that can be

utilized for multiple photonic applications, including band edge and near-infrared lasing,^[21,26] photodetection,^[27,28] fabrication of light-emitting diodes,^[31] security labels,^[32] parity-time symmetric gain–loss systems, where the high contrast is required together with an ability to change the phase shift of the contributing components, or for generating a polarized light source.

In this work, the optical effects induced by superposition of two 1D gratings, comprised of photoluminescent semiconductor material or a metal, were explored. Their fabrication with a low-effort lithography-based approach gives a competitive advantage among other high-resolution techniques. Both gratings were produced on a centimeter-scale area: the metal component was introduced on a rigid substrate through the metal vapor deposition, and the emitter-based grating was printed by the soft-lithographic method on a flexible substrate, to ensure close contact between the structures. A simple stacking and relative in-plane twisting of those 1D grids enabled the robust appearance of fluorescent Moiré patterns that demonstrated chiral photoluminescence without any additional chiral building blocks. This suggests utilizing such structures as functional chiroptical sensors, or in optoelectronic devices, by creating a tunable optical bandgap.

2. Results and Discussion

A typical representation of the Moiré effect is illustrated in **Figure 1**. The supra-periodic pattern is formed by superimposing two 1D gratings (gratings 1 and 2) with the same lattice constant at various relative in-plane rotation angles. Its appearance is then solely defined by geometric parameters of the lattices and relative rotation and can be analytically predicted with high precision (see Figure S1 in the Supporting Information). In its turn, the visibility of the produced supra-periodic pattern depends on the amplitude of the lateral contrast, i.e., the difference between the maximum and minimum luminance of a selected profile. For a complete lateral characterization, one can measure the contrast amplitude along two principal directions: the *M*-axis follows one of the gratings, crossing the Moiré

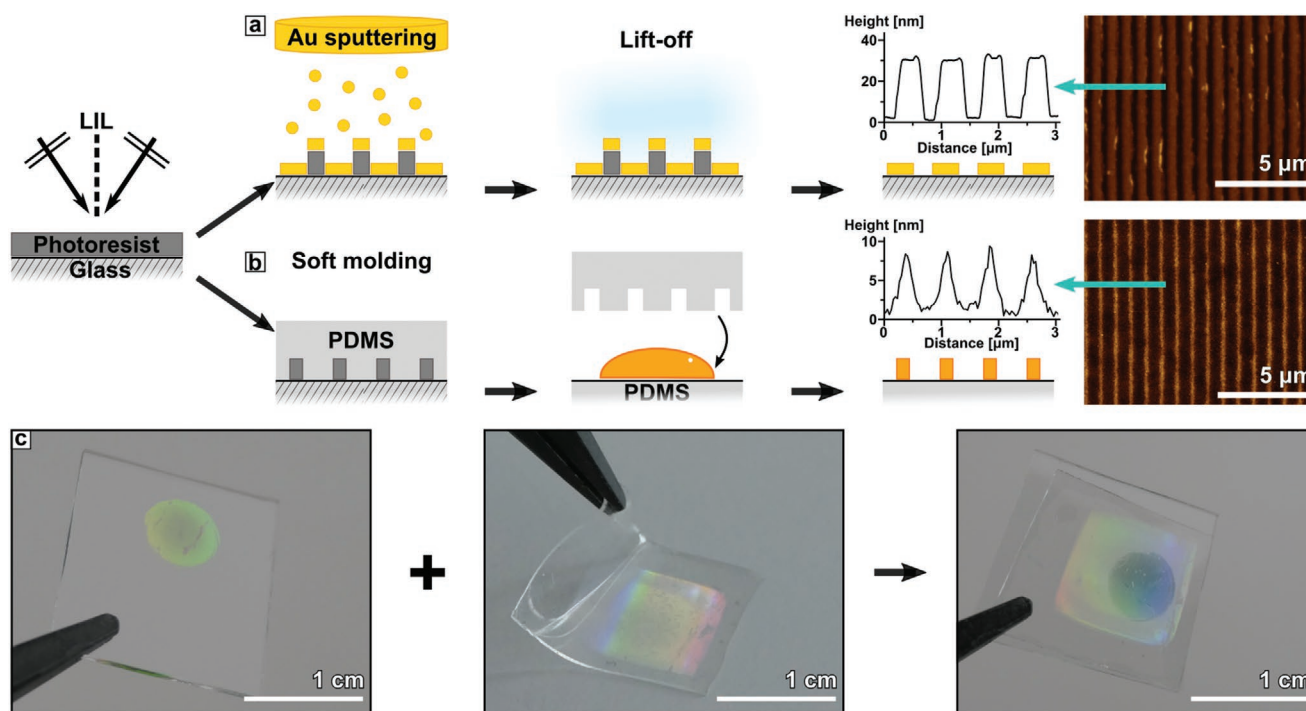


Figure 2. a) Metal grating, fabricated by laser interference lithography (LIL), sputtering of Au, and lift-off process. b) Emitter grating, produced by confinement self-assembly from core-shell quantum emitters with a soft polymer PDMS template. Geometric parameters, determined by AFM: a) periodicity of 790 nm and height of 30 nm, b) periodicity of 820 nm and height of 10 nm. c) Photographs of the metal grating on the glass substrate, superimposed with emitter grating on flexible PDMS substrate.

pattern that appears as a set of interference lines, and the R -axis serves as a reference and goes parallel to the lines of a Moiré pattern. Thus, contrast along the M -axis (C_M) reflects a profile, governed by the Moiré pattern, while C_R shows the contrast profile, dictated by one of the gratings. The Moiré pattern itself is defined through the relative rotation of the two stacked lattices, thus, C_M can be laterally tuned across the large range of distances, since the positions of maximum and minimum intensities are shifted through the changing angle. At the same time, the contrast along the R -direction, being independent of the Moiré pattern, is fixed by the lattice constant.

In further experiments, gratings 1 and 2, having the same lattice constant of ≈ 800 nm, are systematically replaced by one of these materials: gold (Au) or emitting self-assembled semiconductor nanocrystals. To ensure the practical applicability of such gratings, one has to make sure that manufacturing includes low-cost and reproducible techniques. Therefore, laser interference lithography (LIL) and wet-chemical processing were employed. Au periodic structures were obtained after subsequent sputtering and in-solution lift-off process, as described in Figure 2a. Fabrication of the emitter gratings involved polydimethylsiloxane (PDMS) soft molding process, as represented in Figure 2b. A defined volume of nanocrystals was then drop-casted on the flexible substrate, followed by applying the PDMS master template and drying under pressure (flexibility of at least one of the substrates is required to bring the gratings in close contact with each other and ensure the near-field energy transfer). The periodic structure was exposed after peeling-off the PDMS master. Both gratings were characterized by atomic force microscopy (AFM), revealing

periodic structures with uniform geometric parameters over a large scale (see Figure 2c).

Moiré interference effects were first compared between various combinations of periodic structures at the same angle (see Figure 3): emitter and emitter (E&E), metal and metal (M&M), and metal and emitter (M&E). A single, emitter-only grating was used as a reference. The photoluminescent signal was captured by confocal fluorescent microscopy (CFM) imaging under the excitation of 405 nm laser that selectively excited the quantum emitters. In such a configuration, metal grating appeared as dark background, since the reflected excitation light was filtered out and the fluorescence of bulk Au was not detected. To observe the interference of M&M structure, 640 nm laser was used, and the reflected light was collected by the CFM setup. According to the abovementioned formalism of principal axes, to characterize the lateral contrast in various grating combinations, the axes were assigned in the following way: the M -axis always followed the line of assembled QDs in E&E, M&E, and emitter-only gratings, or one of the Au lines in the M&M combination, while the R -axis was parallel to the lines of the Moiré pattern. It is important to note that R and M are not perpendicular to each other and their orientation depends on the relative rotation of the gratings.

To characterize the lateral contrast along R - and M -directions, the following notions were used: single emitter grating was considered as a contrast reference with a maximum intensity value C_0 measured along the M -axis and corrected to the background signal. The contrast C was calculated as the difference between the maximum and minimum value, normalized to C_0 for both directions. The contrast ratio C_M for the emitter grating only

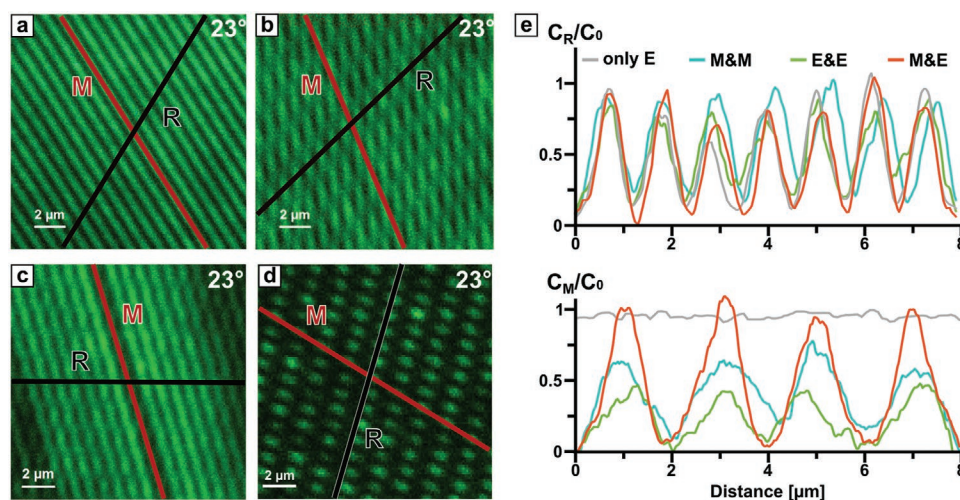


Figure 3. Various combinations of metal and emitter gratings with a fixed lattice constant (≈ 800 nm) and relative rotation angle ($\approx 23^\circ$). a) CFM image of an emitter grating only. The drawn R- and M-axes (shown in black and red lines) indicate principal directions to characterize the contrast amplitude. b–d) CFM images of superimposed metal (b), emitter (c) gratings as well as (d) a combination of both. e) The intensity profiles along R- and M-directions for the various cases. The intensity was shifted to 0 for clarity and normalized to the reference value C_0 -intensity signal, recorded from the emitter grating only.

was then considered as an error rate of 11% for all the following measurements. Along the R-axis, parallel to the Moiré lines, the contrast was comparable within all four samples, resembling the contrast produced by one of the gratings. Following the intensity profile, produced by the Moiré interference, the contrast of $\approx 70\%$ can be achieved for combined identical gratings. However, when stacking absorbing and emitting counterparts, the contrast can be improved by 30% and is comparable to the contrast of only a single emitter grid (exact C_M and C_R values are given in Section T3 in the Supporting Information). This combination allows for high-contrast patterns, where the positions of high/low intensity are not strictly fixed and can be tuned through the in-plane twisting of the superimposed substrates, as demonstrated in Figure 4.

Such a simple approach enables obtaining varied intensity profiles of different periodicities within one structure

(as shown in Figure 4b). Those patterns are defined by the Moiré supra-periodicity and can be as twice as small, or far higher than the initial lattice constant (see Equation (S1) in the Supporting Information), with the lateral resolution limit reaching $\frac{\lambda}{\pi NA} \approx 143$ nm, where $\lambda = 405$ nm represents the central wavelength of the laser and $NA = 0.9$.

Besides lateral contrast, one can consider it in a vertical direction by changing the spacing between metal and emitter gratings. For sensor applications these distance investigations are important, because the analyte layer can be placed at the most sensitive point between the grids. Thus, for a proof of concept, a transparent polymer film of polymethyl-methacrylate (PMMA) spacer was introduced in between the two gratings (Figure 5).

The contrast was maintained in the range of several hundreds of nanometers that is within at least half of the vertical

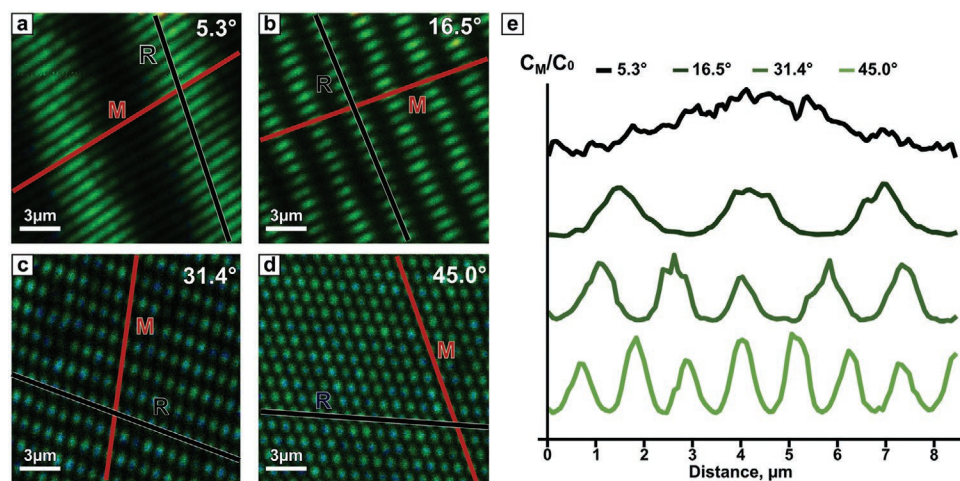


Figure 4. Interference pattern of a superimposed metal and emitter lattices at different angles of orientation. a–d) CFM images at 5.3° , 16.5° , 31.4° , and 45.0° relative rotation angles, respectively, as well as e) the corresponding intensity profiles of the Moiré interference pattern.

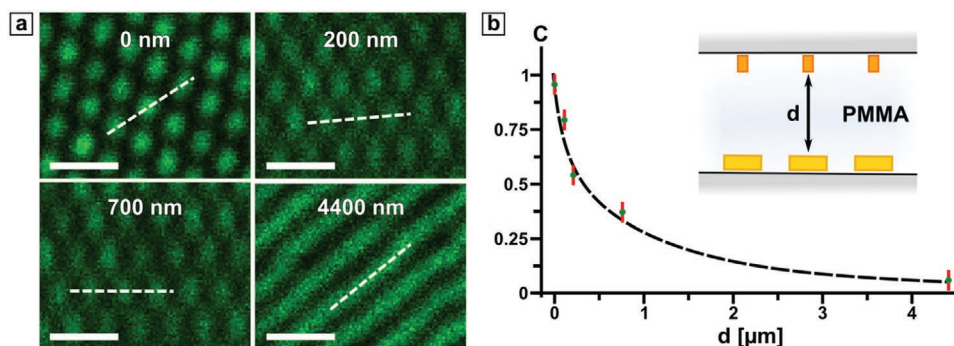


Figure 5. Implementation of a PMMA spacer material to study the interaction depth between the metal and emitter lattice. a) The CFM images show the Moiré interference at spacer distances between 100 nm and 4.4 μm. The contrast C was measured along the white dotted line that follows one of the emitter lines and crosses the lines of the Moiré pattern, if visible. The scale bar is 2 μm. b) The contrast with respect to the spacer thickness. The error is indicated by the red vertical line.

resolution of the objective, estimated as $\frac{2n\lambda}{NA^2} \approx 1490$ nm, with the refractive index n of PMMA being 1.49. It was sufficient to observe the Moiré pattern, even with more than a two-fold decrease in contrast. The change of contrast amplitude with the interlattice distance (as shown in Figure 5b) features power-law decay and supports the near-field nature of the observed interaction. Moreover, the contrast quality was maintained even on the flexible substrate that was constantly prone to mechanical deformations over five months of sample utilization.

The considered configuration of two 1D gratings with a possibility of an arbitrary in-plane rotation also suggests its benefit for creating an emitter-based circular polarizer, since superposition of similar, but only metal-based structures demonstrated strong CD effect.^[11] In our case, however, it implies the transformation of linearly polarized excitation light to the circularly polarized emission. This chiroptical effect was measured and quantitatively evaluated as a degree of polarization at the maximum emission wavelength $g_{PL} = \frac{2(I_{RCP} - I_{LCP})}{(I_{RCP} + I_{LCP})}$, where

$I_{RCP/LCP}$ are the intensities of the detected right (RCP) or left circularly polarized (LCP) emission light, respectively. Spectral analysis of the output light, presented in Section T2 in the Supporting Information, revealed the absence of a spectral shift in the emission of stacked M&E and E&E which allowed to consider the intensity values at the same wavelength of 608 nm. The experimental setup is shown in Figure 6a. The sample was excited at a normal incidence with a continuous p-polarized laser at 405 nm and the photoluminescence signal was collected in the forward direction after passing through a zero-order quarter-wave plate and a linear polarizer to dissect right and left polarization. The RCP and LCP emission intensities of two types of hybrid structures, M&E and E&E, were measured for several in-plane rotation angles, as summarized in Figure 6b.

When the emitter lines were combined with the metal grating, the maximum g_{PL} value of 0.19 was observed for 45° angle of relative rotation between the crossed lines, together with the comparable negative value -0.16 for -45° . Interestingly, the intrinsic chirality of the structure, where two emitter gratings are superimposed, is not only able to give rise of circularly polarized emission but also demonstrates remarkably high g_{PL} -factors: 0.64 and -0.72 for the left and right rotation of the

stacked gratings, respectively. The absence of perfect symmetry for the opposite rotations was possibly caused by slightly mismatched angles and geometrical variations within the gratings. The obtained values are comparable with the ones reported so far in the literature, where achiral QDs were combined with the chiral metal template: 0.34 for the ion-beam patterned gold film^[16] and 0.95 when less lossy silver nanoarcs were employed.^[17] The suggested structure is, on the other hand, completely loss-free and features low-effort self-assembly of colloidal QDs that can be used as a compact circular polarizer for on-chip photonic circuits and benefit as a component for an optical isolator.

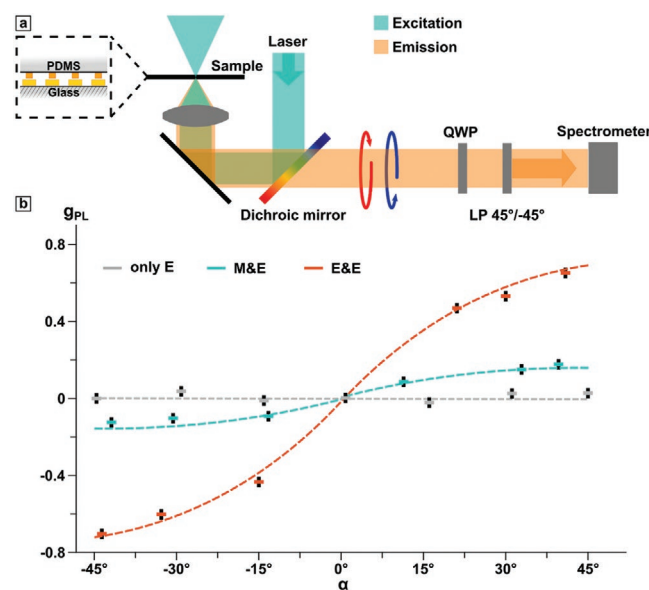


Figure 6. Measurement of polarized photoluminescence. a) Experimental setup shows the laser excitation (polarization of the beam is shown with a blue arrow and the direction of propagation with pink) and analysis of the reflected light using a $\lambda/4$ wave plate (QWP) and linear polarizer (LP) that is oriented at 45° or -45° to the fast axis of the QWP. b) The g_{PL} -factor at 608 nm with respect to various orientation angles for superimposed gratings. The error rate of 0.008, marked as a vertical black line, was measured as the degree of polarization of only the emitter grating.

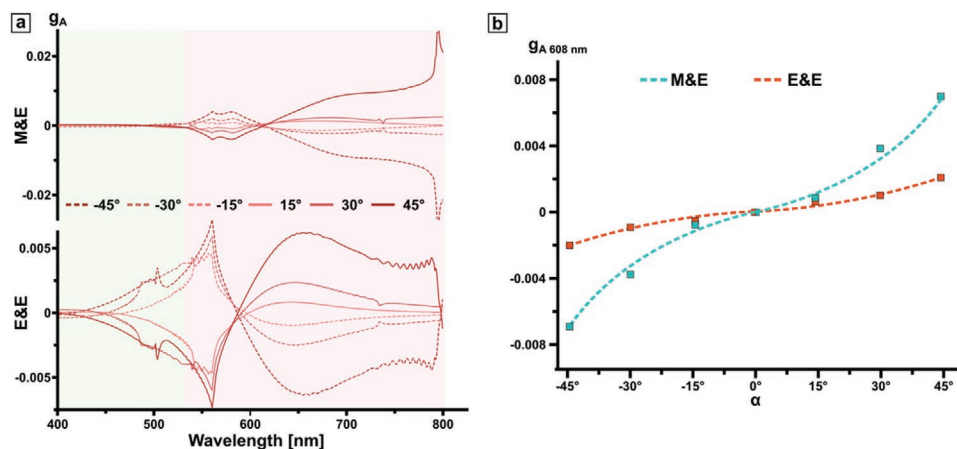


Figure 7. Electromagnetic simulations of polarized photoluminescence. a) The chiral response of stacked M&E and E&E at several complementary angles α between -45° and 45° . Absorption and emission bands of the QDs are shown in light green and red respectively. b) The g_A -factor, measured at the maximum emission wavelength, with respect to various orientation angles for superimposed gratings.

To get further insight into the origin of the chiral response for those stacked structures, finite-difference time-domain (FDTD) simulations were performed (described in detail in Section T5 in the Supporting Information). In contrast to the experimental setup, where the structures were illuminated by the linearly polarized light and the chiral emission was detected, here both configurations were studied under the circularly polarized light, differentiating between the absorption ($A_{\text{RCP/LCP}}$) of RCP or LCP light. The degree of polarization was then estimated as $g_A = \frac{2(A_{\text{RCP}} - A_{\text{LCP}})}{(A_{\text{RCP}} + A_{\text{LCP}})}$.

The latter allows for uncovering the relation between the intrinsic circular dichroism of the crossed-bar-structures and the spectral properties of the emitter. As shown in Figure 7a, both stacked M&E and E&E structures demonstrate a mirror symmetry of the CD response for the opposite angles. Both combinations show a resonance near the maximum emission wavelength of the QDs that is characterized by crossing the zero g_A -value. The strongest CD signal corresponds the first and second diffraction orders at normal incidence (800 nm in air, and 560 nm in PDMS) that suggests the possible origin of chiral properties from the diffractive channels. Simulating CD effect in absorption gives further insight into the nature of the chiral emission: the strongest response matches the spectral region of photoluminescence that is in accordance with the results from one of the earlier reports.^[17] Moreover, the broad emission spectrum of QDs allows for a broad wavelength range of the dichroic effect.

3. Conclusion

In conclusion, we propose a robust method for large-area manufacturing of light-emitting periodic 1D structures. When combined with a similar, but composed of light-absorbing gold, grating, the rising Moiré interference effect enables to achieve contrast values, significantly higher than when using material-wise identical gratings. The observed effect can be easily tuned over the micrometer-range distance and maintained for large

interlattice separation that opens up a possibility to replace the spacer with various functional materials, such as photosensitive polymers,^[33] activated at the QDs emission wavelength, or electrically conductive resins,^[34] to extend the discussed concept to stimuli-responsive metasurfaces. Moreover, such spatially controllable, yet strong contrast can be further employed for security labeling,^[32] taking the advantage of the simplicity of mass production and optical durability. On the other hand, Moiré's combination of two emitter gratings allows for a strong photoluminescent chiroptical effect. It demonstrates, for the first time, a reconfigurable chiral arrangement of semiconductor QDs without the need for supplementary chiral building blocks. To further increase the degree of polarization, one can benefit from the colloidal self-assembly approach and change the lattice geometry simply by designing a different stamp to introduce more hybridization states or implement additional emitter-based or plasmonic 1D gratings into the structure to obtain a more complex lattice overlay.^[35,36] Moreover, one can confine the proposed chiral Moiré system within a nanocavity, taking the advantage of fluorescent enhancement.^[37]

4. Experimental Section

Laser Interference Lithography (LIL): To produce a structured film on the glass substrate, laser interference lithography was employed. Right before use, microscopy glass slides were divided into individual pieces (2×2 cm) and cleaned with isopropyl alcohol and ultrapure water in a 1:1 ratio by sonication for 20 min at 37 kHz. Positive photoresist (mr-P 1202LIL, Microresist Technology GmbH, Germany) was spin-coated onto the cleaned and dried under a stream of nitrogen substrate. Optimized spin parameters of 3000 rpm, acceleration of 1000 rpm s^{-1} , and total spin time of 33 s produced a thin film of 185 nm thickness, as confirmed by spectroscopic ellipsometry (RC2-DI, J.A. Woollam Co., Inc.). The coated substrates were baked at 95°C for 60 s and further exposed to the 325 nm laser with a dose of 12 mJ cm^{-2} . The backside of the substrate was covered with black adhesive tape to avoid unnecessary reflections. To develop the exposed photoresist, the sample was submerged into the developer (mr-D 374/S, Microresist Technology GmbH, Germany) for 2 min, rinsed with ultrapure water, and dried under a stream of nitrogen.

Fabrication of Gold Gratings: To fabricate a metal grating, a structured photoresist film was sputtered with gold at 20 rpm rotation speed with 0.1 nm s^{-1} until the thickness of 35–40 nm was achieved. The sacrificial photoresist was then dissolved with acetone and sonication at $45 \text{ }^\circ\text{C}$, 37 kHz for 15 s.

Synthesis of Quantum Dots: AgInS/ZnS core/shell QDs were prepared in aqueous alkaline solutions as described in detail in earlier works.^[19,30] In short, AgInS core was formed via breaking the Ag(I) and In(III) complexes with thioglycolic acid (TGA). A ZnS shell was then overgrown over the AgInS core by the addition of a Zn(II)–TGA complex. The formed QDs were then purified by centrifugation and redispersed in pure DI water. The final molar concentration of nanocrystals is determined through Ag(I) concentration, being 0.1 M. The atomic ratio of metals in the final AgInS/ZnS particles was kept at Ag/In/Zn = 1:4:8. The average size of the synthesized particles was reported to be 2–3.5 nm.^[19] Further insight into the optical properties of QDs is given in Section T2 in the Supporting Information.

Soft Lithographic Fabrication of QD Grating: Produced by LIL, the structured film of a photoresist was replicated using an elastomeric silicone kit (Sylgard 184, Dow Chemicals, USA) with a ratio of prepolymer and catalyst of 10:1 to create the mold. The resulting mold was trimmed and fused by plasma treatment to an elastomeric silicone film in a petri dish. Right before use, the replica was immersed in 2 M hydrochloric acid for 30 min, rinsed with water, and dried under a stream of nitrogen to create a sufficiently hydrophilic surface. In the next step, 4 μL of a water-based dispersion of the colloidal solution (TGA-capped AgInS/ZnS QDs) was placed on a flat target substrate. The hydrophilized mold was placed on the quantum dot dispersion and 750 g of weights were placed on the Petri dish to ensure close contact between the mold and the flat surface. The assembly was dried for eight hours at room temperature and relative humidity of 32%. The stamp was then removed by peeling off. The quantum yield (QY) of the assembled structures was estimated up to 25% (see Section T2 in the Supporting Information).^[38]

Confocal Fluorescence Microscopy: Confocal fluorescence microscopy (CFM) measurements were acquired with an inverted confocal scanning microscope (MicroTime 200, PicoQuant, Germany) with a 100 \times air objective (UPLFLN, NA 0.9, Olympus, Japan). For excitation, a picosecond pulsed p-polarized laser diode source (LDH-D-C-405, PicoQuant, Germany) with a center wavelength of 405 nm and a pulse width of 110 ps (full width at half-maximum, FWHM), driven at a repetition rate of 0.5 MHz. For fluorescence collection, a dichroic mirror (ZT405-442/510rpc-UF3, Chroma, USA), a long pass filter with a cut-off below 425 nm (FF01-519/LP, Shamrock, USA) and a single photon counting module (SPCM-AQRH, Excelitas, USA) were used. For evaluation, SymphoTime 64 2.3 was used. For spectroscopy measurements, the sample was excited under a constant illumination at 405 nm and the signal was recorded by the spectrometer Newton 920 (Oxford Instruments, UK). For time-correlated single-photon counting (TCSPC), a single-photon counting module (SPCM-AQRH, Excelitas, USA) was used. The lifetime was then calculated by SymphoTime 64 2.3. Fluorescence life time images were recorded at 1 μW excitation power (before objective) and a dwell time of 2 ms per pixel.

Finite-Difference Time-Domain (FDTD) Simulations: A commercial-grade simulator based on the finite-difference time-domain (FDTD) method is used to perform the calculations (FDTD: 3D electromagnetic simulator).^[39] To simulate the optical response, two total-field scattered-field sources ($\lambda = 400\text{--}800 \text{ nm}$) were used, illuminating the structure at a normal incidence with a relative phase shift of 90° or -90° for right- and left-circularly polarized light. Perfectly matching layer boundary conditions were used in the Y-direction, and periodic boundary conditions were used along X- and Z-axes. The grating lines were represented by parallelepipeds with the dimensions, matching the ones, experimentally measured with atomic force microscopy. To obtain the optical responses of the system, frequency-domain field monitors were used. The frequency points were matching the wavelength span of the source. For the dielectric properties of gold, data from Johnson and Christy were fitted using six coefficients, with a root-mean-square (RMS) error of 0.25. For QDs, a Lorentz oscillator model was employed, with a

resonance wavelength at the emission maximum of the QDs (608 nm) and a linewidth of 110 nm, matching the actual spectral width of the emission band. For the best simulation stability, the mesh area was set around the existing structure in all three principal directions with a mesh step size of 1 nm and the auto-shutoff level was set to 10^{-7} .

Moiré Interference Measurements: To obtain Moiré interference pattern, the substrates need to be stacked with the structure side facing each other. The soft elastomeric substrate has to be pressed onto the glass substrate to ensure the close contact between the gratings. For the distance-dependent measurements, polymethyl methacrylate (PMMA A2 950 kDa, Microchemicals GmbH, Germany) was spin-coated at 1000 rpm for 60 s, followed by soft-baking at $180 \text{ }^\circ\text{C}$ for 60 s that resulted in a transparent polymeric film with the thickness of approximately 100 nm, determined by spectroscopic ellipsometry (RC2-D1, J.A. Woollam Co., Inc.). For larger film thicknesses, the latter was repeated up to maximum total thickness of approximately 4.4 μm . For the comparative contrast measurements, when two identical metal gratings are combined, index matching oil was applied between two glass substrates. In this case, the stacked structures were illuminated with a 640 nm laser and the reflected light was not filtered out.

Surface Characterization: Produced line structures were imaged by atomic force microscopy (AFM). The scanning was performed in the tapping mode with silicon nitride probes (typical resonant frequency in air: 296 kHz). Amplitude set point was adjusted within the range of 100–200 mV at the scanning frequency 0.5–1 Hz.

Supporting Information

Supporting Information is available from the Wiley Online Library or from the author.

Acknowledgements

O.A. and M.S. contributed equally to this work. The authors would like to acknowledge Alexandra Raevskaya and Oleksandr Stroyuk for the synthesis of the core-shell quantum dot emitters and Benjamin Kohn for proofreading the manuscript. This project was financially supported by the Volkswagen Foundation through a Freigeist Fellowship to TAFK. For Open Access, the project was funded by the Deutsche Forschungsgemeinschaft (DFG, German Research Foundation) under Grant No. 404818834.

Open access funding enabled and organized by Projekt DEAL.

Conflict of Interest

The authors declare no conflict of interest.

Keywords

circular dichroism, Moiré effect, photoluminescence, self-assembled nanoparticles, soft-lithography

Received: July 29, 2020

Revised: November 12, 2020

Published online: December 13, 2020

[1] I. Amidror, *The Theory of the Moiré Phenomenon*, Springer, London 2009.

[2] S. Kishimoto, M. Egashira, N. Shinya, *Opt. Eng.* **1993**, 32, 522.

- [3] J. K. Drinkwater, B. W. Holmes, K. A. Jones, *Proc. SPIE* **2000**, 3973, 66.
- [4] Z. Wu, G. Kelp, M. N. Yogeesh, W. Li, K. M. McNicholas, A. Briggs, B. B. Rajeeva, D. Akinwande, S. R. Bank, G. Shvets, Y. Zheng, *Nanoscale* **2016**, 8, 18461.
- [5] S. Balci, A. Kocabas, C. Kocabas, A. Aydinli, *Appl. Phys. Lett.* **2011**, 98, 031101.
- [6] S. M. Lubin, W. Zhou, A. J. Hryn, M. D. Huntington, T. W. Odom, *Nano Lett.* **2012**, 12, 4948.
- [7] C. Jin, B. C. Olsen, E. J. Luber, J. M. Buriak, *ACS Nano* **2017**, 11, 3237.
- [8] K. Chen, B. B. Rajeeva, Z. Wu, M. Rukavina, T. D. Dao, S. Ishii, M. Aono, T. Nagao, Y. Zheng, *ACS Nano* **2015**, 9, 6031.
- [9] L. A. Ibbotson, A. Demetriadou, S. Croxall, O. Hess, J. J. Baumberg, *Sci. Rep.* **2015**, 5, 8313.
- [10] W. Gao, H. M. Leung, Y. Li, H. Chen, W. Y. Tam, *J. Opt.* **2011**, 13, 115101.
- [11] J.-G. Yun, S.-J. Kim, H. Yun, K. Lee, J. Sung, J. Kim, Y. Lee, B. Lee, *Opt. Express* **2017**, 25, 14260.
- [12] V. Gupta, P. T. Probst, F. R. Goßler, A. M. Steiner, J. Schubert, Y. Brasse, T. A. F. König, A. Fery, *ACS Appl. Mater. Interfaces* **2019**, 11, 28189.
- [13] V. Lesnyak, N. Gaponik, A. Eychmüller, *Chem. Soc. Rev.* **2013**, 42, 2905.
- [14] Y. Shirasaki, G. J. Supran, M. G. Bawendi, V. Bulović, *Nat. Photonics* **2013**, 7, 13.
- [15] X. Gao, B. Han, X. Yang, Z. Tang, *J. Am. Chem. Soc.* **2019**, 141, 13700.
- [16] Z. Wang, Y. Wang, G. Adamo, J. Teng, H. Sun, *Laser Photonics Rev.* **2019**, 13, 1800276.
- [17] S. P. Rodrigues, Y. Cui, S. Lan, L. Kang, W. Cai, *Adv. Mater.* **2015**, 27, 1124.
- [18] M. Noh, T. Kim, H. Lee, C.-K. Kim, S.-W. Joo, K. Lee, *Colloids Surf., A* **2010**, 359, 39.
- [19] A. Raevskaya, V. Lesnyak, D. Haubold, V. Dzhagan, O. Stroyuk, N. Gaponik, D. R. T. Zahn, A. Eychmüller, *J. Phys. Chem. C* **2017**, 121, 9032.
- [20] F. Prins, D. K. Kim, J. Cui, E. De Leo, L. L. Spiegel, K. M. McPeak, D. J. Norris, *Nano Lett.* **2017**, 17, 1319.
- [21] V. Reboud, P. Lovera, N. Kehagias, M. Zelsmann, C. Schuster, F. Reuther, G. Gruetzner, G. Redmond, C. M. Sotomayor Torres, *Appl. Phys. Lett.* **2007**, 91, 151101.
- [22] T. S. Mentzel, D. D. Wanger, N. Ray, B. J. Walker, D. Strasfeld, M. G. Bawendi, M. A. Kastner, *Nano Lett.* **2012**, 12, 4404.
- [23] M. Tagliazucchi, V. A. Amin, S. T. Schneebeli, J. F. Stoddart, E. A. Weiss, *Adv. Mater.* **2012**, 24, 3617.
- [24] S. T. Malak, G. Liang, R. Thevamaran, Y. J. Yoon, M. J. Smith, J. Jung, C. H. Lin, Z. Lin, E. L. Thomas, V. V. Tsukruk, *J. Phys. Chem. C* **2017**, 121, 13370.
- [25] J. Yang, M. K. Choi, D.-H. Kim, T. Hyeon, *Adv. Mater.* **2016**, 28, 1176.
- [26] Z. Zhang, Z. Wang, Z. Xu, Q. Gao, P. Liu, J. Ren, M. Li, C. Zhou, Q. Liao, H. Fu, *Adv. Opt. Mater.* **2018**, 6, 1800219.
- [27] Z. Dai, Q. Ou, C. Wang, G. Si, B. Shabbir, C. Zheng, Z. Wang, Y. Zhang, Y. Huang, Y. Dong, J. J. Jasieniak, B. Su, Q. Bao, *J. Mater. Chem. C* **2019**, 7, 5954.
- [28] B. Jeong, H. Han, H. H. Kim, W. K. Choi, Y. J. Park, C. Park, *ACS Nano* **2020**, 14, 1645.
- [29] L. Kim, P. O. Anikeeva, S. A. Coe-Sullivan, J. S. Steckel, M. G. Bawendi, V. Bulović, *Nano Lett.* **2008**, 8, 4513.
- [30] O. Stroyuk, A. Raevskaya, F. Spranger, O. Selyshchev, V. Dzhagan, S. Schulze, D. R. T. Zahn, A. Eychmüller, *J. Phys. Chem. C* **2018**, 122, 13648.
- [31] H. H. Kim, J. W. Shim, Y.-J. You, Y. J. Lee, C. Park, D. K. Hwang, W. K. Choi, *J. Mater. Chem. C* **2017**, 5, 1596.
- [32] Y. Liu, F. Han, F. Li, Y. Zhao, M. Chen, Z. Xu, X. Zheng, H. Hu, J. Yao, T. Guo, W. Lin, Y. Zheng, B. You, P. Liu, Y. Li, L. Qian, *Nat. Commun.* **2019**, 10, 1.
- [33] J. Jelken, S. Santer, *RSC Adv.* **2019**, 9, 20295.
- [34] G. Scordo, V. Bertana, L. Scaltrito, S. Ferrero, M. Cocuzza, S. L. Marasso, S. Romano, R. Sesana, F. Catania, C. F. Pirri, *Mater. Today Commun.* **2019**, 19, 12.
- [35] M. Mayer, M. J. Schnepf, T. A. F. König, A. Fery, *Adv. Opt. Mater.* **2019**, 7, 1800564.
- [36] P. Probst, M. Mayer, V. Gupta, A. M. Steiner, Z. Ziwei, G. Auernhammer, T. A. F. König, A. Fery, unpublished, **2020**.
- [37] F. R. Goßler, A. M. Steiner, O. Stroyuk, A. Raevskaya, T. A. F. König, *J. Phys. Chem. C* **2019**, 123, 6745.
- [38] M. J. Schnepf, Y. Brasse, F. R. Goßler, A. M. Steiner, J. Obermeier, M. Lippitz, A. Fery, T. A. F. König, *Z. Phys. Chem.* **2018**, 232, 1593.
- [39] FDTD Solutions, Lumerical Inc., <https://www.lumerical.com/products/fdtd-solutions/> (accessed: November 2020).